

W. PIEKARSKA\*, M. KUBIAK\*, A. BOKOTA\*\*

## NUMERICAL SIMULATION OF THERMAL PHENOMENA AND PHASE TRANSFORMATIONS IN LASER-ARC HYBRID WELDED JOINTS

### ANALIZA NUMERYCZNA ZJAWISK CIEPLNYCH I PRZEMIAN FAZOWYCH W POŁĄCZENIACH SPAWANYCH HYBRYDOWO LASER-ŁUK ELEKTRYCZNY

The paper concerns mathematical and numerical modelling of temperature field with convective motion of liquid metal in the melted zone taken into account and numerical estimation of structure composition of a plate made of S355 steel, butt-welded by laser-arc hybrid welding technique. Coupled transport phenomena, including heat transfer and fluid flow in the melted zone, were described respectively by transient heat transfer equation with convective term and Navier-Stokes equation. Latent heat associated with the material's state changes and latent heat of phase transformations in solid state were taken into consideration in the solution algorithm. The kinetics of phase transformations and volumetric fractions of arising phases were calculated on the basis of the Johnson-Mehl-Avrami (JMA) and Koistinen-Marburger (KM) classic mathematical models. In modelling of phase transformations during heating continuous heating transformation (CHT) diagram was used, whereas continuous cooling transformation (CCT) diagram was used in modelling of phase transformations during cooling of welded steel.

Transient heat transfer equation was solved using finite element method in Petrov-Galerkin formulation and Navier-Stokes equation was solved in Chorin's projection method. The solution algorithms were implemented in ObjectPascal programming language.

**Keywords:** Laser-arc hybrid welding, heat transfer, fluid flow, phase transformations, structure composition, numerical modelling

Praca zawiera numeryczne modelowanie pola temperatury oraz prognozowanie numeryczne składu strukturalnego płaskownika wykonanego ze stali S355, spawanego doczołowo techniką hybrydową laser-łuk elektryczny. Model pola temperatury uwzględnia ruch ciekłego metalu w jeziorku spawalniczym. Sprzężone zjawiska transportu ciepła i cieczy w strefie przetopienia opisywane są równaniem nieustalonego przewodzenia ciepła z członem konwekcyjnym i równaniem Naviera-Stokesa. W algorytmie numerycznym uwzględniono ciepła związane ze zmianą stanu skupienia materiału i ciepła przemian fazowych w stanie stałym. Kinetykę przemian fazowych w stanie stałym oraz algorytmy numeryczne wyznaczania ułamków objętościowych powstających faz oparto na równaniach Johnsona-Mehla-Avramiego (JMA) i Koistinena-Marburgera (KM). W modelowaniu przemian nagrzewania wykorzystano wykres ciągłego nagrzewania (CTPc<sup>A</sup>), natomiast w modelowaniu przemian chłodzenia wykorzystano spawalniczy wykres przemian austenitu (CTPc-S) spawanej stali.

Do rozwiązania równania nieustalonego przewodzenia ciepła zastosowano metodę elementów skończonych w sformułowaniu Petrov-Galerkina, a równanie Naviera-Stokesa rozwiązano metodą projekcji Chorina. Algorytmy analizy rozważanych zagadnień zaimplementowano w języku programowania ObjectPascal.

### 1. Introduction

Laser – arc hybrid welding process combines popular and well-known arc welding method with laser beam welding. This technology is recently under particular investigations [1-5]. The use of two heat sources in a single welding process contributes to improvements in weld quality even at very high welding speeds.

The effect of metal heating during hybrid welding mostly depends on the amount and distribution of heat load generated by two coupled heat sources: electric arc and laser beam. Heat transfer and convective motion of liquid material in the welding pool determine the size and geometry of the weld.

Appropriate use and optimization of this welding technique requires a large number of technological pa-

\* CZĘSTOCHOWA UNIVERSITY OF TECHNOLOGY, INSTITUTE OF MECHANICS AND MACHINE DESIGN FOUNDATIONS, 42-200 CZĘSTOCHOWA, 73 DĄBROWSKI STR., POLAND

\*\* CZĘSTOCHOWA UNIVERSITY OF TECHNOLOGY, INSTITUTE OF COMPUTER AND INFORMATION SCIENCES, 42-200 CZĘSTOCHOWA, 73 DĄBROWSKI STR., POLAND

rameters that should be correctly set to achieve stable process, and also understanding the complex thermal phenomena occurring during welding of steel. In most cases of research involving hybrid welding the attention is paid to experimental study of effective way to combine laser beam and electric arc welding methods. Studies concerning mathematical and numerical modelling of hybrid welding process, appearing in the last few years, are mainly based on the solutions used in modelling of autonomous laser welding or arc welding processes [6-12].

The temperature distribution is important in modelling of thermal phenomena because the shape of the weld, structure composition and mechanical properties of welded joint depends on it. The weld and the region adjacent to the weld are heated to various temperatures depending on the distance from the centre of heat sources activity zone.

Different heating and cooling conditions during welding contribute to appearing of various structures in the weld which leads to the different mechanical properties of the joint. The concentration of heat and high cooling rates occurring during the welding lead to appearing of hardening structures in the weld and heat affected zone (HAZ). That is why the determination of the kinetics of phase transformations for analyzed steel is important in numerical modelling, because reliable determination of the kinetics allows for forecasting the structure composition in welded joints. Knowledge about the structural heterogeneity of welded joints is important during construction design.

In the research concerning modelling of hybrid welding process, analyzed physical phenomena include: the movement of liquid material in the melted zone, mixing of the weld material with electrode material, dynamics of the electrode droplet flowing into the welding pool and flow through the porous medium [7, 8, 10]. The computational models are often simplified in practice, to represent the most important phenomena which have a major influence on shape, size and mechanical properties of welded joints [6, 11, 12].

This paper concerns mathematical and numerical modelling of temperature field with convective motion of liquid metal in the welding pool taken into account, and also numerical estimation of structure composition of laser-arc hybrid welded joint. Coupled heat transfer and fluid flow phenomena are determined on the basis of numerical solution of transient heat transfer equation with convective term and Navier-Stokes equation with natural convection and flow through porous medium taken into account. Latent heat associated with material's state changes and latent heat of phase transformations in solid state are taken into account in the solution al-

gorithm. The kinetics of phase transformations in solid state as well as the volumetric fractions of arising structure constituents are obtained by the solution of Johnson-Mehl-Avrami (JMA) and Koistinen-Marburger (KM) equations. Austenitization temperatures ( $A_{c1}$  and  $A_{c3}$ ) changing with heating rates, reflected in the continuous heating transformation (CHT) diagram were used in the model of phase transformations during heating. On the other hand in modelling of phase transformation during cooling, continuous cooling transformation diagram (CCT) for welded S355 steel was used.

Presented mathematical and numerical models of thermal phenomena allow for the analysis of important technological parameters of laser-arc hybrid welding process, so far mostly determined by experimental research.

## 2. Thermal phenomena

Schematic sketch of considered system is illustrated in figure 1. Heat conduction in welded flat is mostly affected by the power distribution of electric arc ( $Q_1$ ) and laser beam ( $Q_2$ ) heat sources and they relative arrangement as well as welding speed. The following analysis assumes that electric arc and laser beam heat sources are acting in tandem at a specified laser-to-arc distance ( $d$ ). Liquid material flow is mostly driven by the buoyancy in the melted zone, moreover liquid metal motion is assumed as a flow through porous medium in the mushy zone (between solidus and liquidus temperatures). Latent heat of fusion (solid-liquid transformation) in the mushy zone, evaporation (liquid-gas transformation) in temperatures exceeding the metal boiling point and latent heat of phase transformations in solid state between start and final temperatures of every phase were taken into account in considerations.

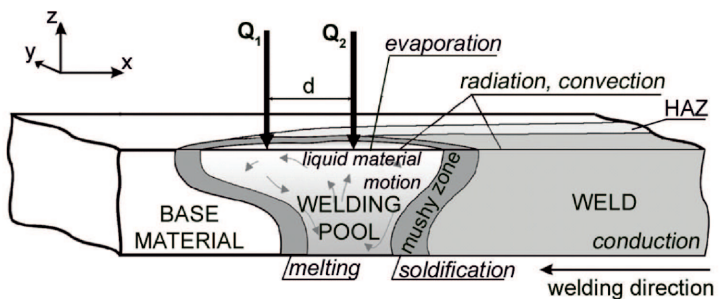


Fig. 1. Schematic sketch of considered system

## 2.1. Governing equations

Temperature field was obtained by the solution of transient heat transfer equation with activity of internal heat sources and convective term taken into account, expressed as follows

$$\nabla \cdot (\lambda \nabla T) = C_{ef} \left( \frac{\partial T}{\partial t} + \nabla T \cdot \mathbf{v} \right) - \tilde{Q} \quad (1)$$

where  $\lambda = \lambda(T)$  is a thermal conductivity,  $C_{ef}$  is the effective heat capacity which includes latent heat of fusion, evaporation and latent heat of phase transformations in solid state [12, 13, 14],  $\tilde{Q} = Q_1 + Q_2$  is a volumetric heat source, where  $Q_1$  is the electric arc heat source and  $Q_2$  is the laser beam heat source,  $\mathbf{v} = \mathbf{v}(\mathbf{x}, t)$  is a velocity vector and  $\mathbf{x} = \mathbf{x}(x_\alpha)$  is a vector of a material point coordinates.

Equation (1) is completed by initial  $t = 0 : T = T_0$  and boundary conditions of Dirichlet, Neumann and Newton type with heat loss due to convection, radiation emission and evaporation taken into account [13, 14]

$$T|_\Gamma = \tilde{T}, \quad q = -\lambda \frac{\partial T}{\partial n} \Big|_\Gamma = \tilde{q} \quad (2)$$

$$-\lambda \frac{\partial T}{\partial n} = -q_o^+ \alpha_k (T|_\Gamma - T_0) + \varepsilon \sigma (T^4 - T_0^4) + q_v \quad (3)$$

where  $\alpha$  is a convective coefficient,  $\varepsilon$  is a radiation coefficient and  $\sigma$  is Stefan - Boltzmann constant. Term  $q_0$  is a heat flux towards the top surface of the welded element ( $z = 0$ ) in the source activity zone, while  $q_v$  represents heat loss due to material evaporation in area where  $T \geq T_L$ ,  $\Gamma$  is a boundary of analysed domain.

Equation (1) was solved using finite element method (FEM) [15]. The solution formula is a result of weighed residuum criterion leading to the weak form

$$\int_{\Omega} \varphi [\nabla \cdot (\lambda \nabla T) + \tilde{Q}] d\Omega = \int_{\Omega} \varphi C_{ef} \left( \frac{\partial T}{\partial t} + \nabla T \cdot \mathbf{v} \right) d\Omega \quad (4)$$

where  $\varphi = \varphi(\mathbf{x})$  is a weigh function.

Temperature in every node of FE mesh is time function  $T_j = T_j(t)$ , time integration of equation (4) leads to the following formula

$$\begin{aligned} \sum_e \left( \tilde{K}_{ij}^e + V_{ij}^e \right) \int_t \vartheta(t) T_j(t) dt + \sum_e \tilde{M}_{ij}^e \int_t \vartheta(t) \frac{\partial T_j(t)}{\partial t} dt = \\ = \sum_e S_{ij}^e \int_t \vartheta(t) Q_j^e(t) dt - \sum_{e|\Gamma} S_{ij}^\Gamma \int_t \vartheta(t) \tilde{q}_j^e(t) dt \end{aligned} \quad (5)$$

where  $\vartheta = \vartheta(t)$  is time weight function,  $V_{ij}^e$  is local convection matrix,  $S_{ij}^e$  is local matrix of coefficients,  $Q_j^e(t)$  is local vector of internal heat sources,  $\tilde{q}_j^e(t)$  is local vector of boundary fluxes.

The final form of solution to the problem, after time integration, is expressed in the following expression

$$\begin{aligned} (\beta K_{ij} + M_{ij}) T_j^{s+1} = & [M_{ij} - (1 - \beta) K_{ij}] T_j^s + \beta Q_i^{s+1} + \\ & + (1 - \beta) Q_i^s - \beta q_i^{*s+1} - (1 - \beta) q_i^{*s} \end{aligned} \quad (6)$$

where  $\beta$  is time integration coefficient,  $M_{ij} = (1/\Delta t^s) \tilde{M}_{ij}$  is a heat capacity matrix,  $K_{ij} = \tilde{K}_{ij} + V_{ij}$  is a conductivity matrix,  $\Delta t^s$  is the actual time step (in time level  $s$ ).

Velocity field of liquid material in the melted zone was obtained by the solution Navier-Stokes equations with convective motion according to Boussinesq's model and fluid flow through porous medium formulated in Darcy's model [7, 8, 14]

$$\frac{\partial(\rho \mathbf{v})}{\partial t} + \nabla \cdot (\rho \mathbf{v} \mathbf{v}) = -\nabla p + \nabla \cdot (\mu \nabla \mathbf{v}) + \rho \mathbf{g} \beta_T (T - T_{ref}) - \frac{\mu}{K} \mathbf{v} \quad (7)$$

where  $\rho$  is a density,  $\mathbf{g}$  is an acceleration of gravity vector,  $\beta_T$  is a volume expansion coefficient due to heating,  $T_{ref}$  is a reference temperature (solidus temperature),  $\mu$  is a dynamic viscosity,  $K$  is porous medium permeability.

Navier-Stokes equation (7), satisfying the mass continuity equation

$$\frac{\partial \rho}{\partial t} + \nabla \cdot (\rho \mathbf{v}) = 0 \quad (8)$$

is completed by initial condition  $t = 0 : \mathbf{v}_0 = 0$  and boundary condition of Dirichlet type,  $\mathbf{v}_b = 0$  implemented at the welding pool boundary.

If solid fraction in the mushy zone is assumed with linear approximation between solidus and liquidus temperatures ( $T_S$  and  $T_L$ ), then

$$f_s = \begin{cases} 1 & \text{for } T < T_S \\ \frac{T_L - T}{T_L - T_S} & \text{for } T_S \leq T \leq T_L \\ 0 & \text{for } T > T_L \end{cases} \quad (9)$$

moreover, if mushy zone is composed of regular matrix of spherical grains submerged in liquid material, the porous medium permeability is given by the Carman – Kozeny equation [8, 14]

$$K = K_0 \frac{f_l^3}{(1 - f_l)^2}; \quad K_0 = \frac{d_0^2}{180} \quad (10)$$

Equation (7) was solved using Chorin's projection with the finite volume method (FVM) [16]. In the first stage of projection, the Navier-Stokes equation is solved without momentum changes due to pressure forces, as follows:

$$\begin{aligned} \frac{\mathbf{v}^* - \mathbf{v}^n}{\Delta t} = \\ = -\nabla \cdot (\mathbf{v} \mathbf{v})^n + \frac{1}{\rho^n} (\mu \nabla^2 \mathbf{v}^n + \rho^n \mathbf{g} \beta_T (T - T_{ref}) - \frac{\mu}{K} \mathbf{v}^n) \end{aligned} \quad (11)$$

where  $\mathbf{v}^*$  is a temporary velocity obtained from changes in velocity  $\mathbf{v}^n$  (in time level  $n$ ) resulting from advection, viscosity and body force terms.

In the second stage, the projection of velocity  $\mathbf{v}^*$  onto  $\mathbf{v}^{n+1}$  is made according to the formula

$$\frac{\mathbf{v}^{n+1} - \mathbf{v}^*}{\Delta t} = -\frac{1}{\rho^n} (\nabla p^{n+1}) \quad (12)$$

The formula (12) with the continuity equation  $\nabla \cdot \mathbf{v} = 0$  is combined into one Poisson equation

$$\nabla \cdot \left( \frac{1}{\rho^n} (\nabla p^{n+1}) \right) = \frac{1}{\Delta t} \nabla \cdot \mathbf{v}^* \quad (13)$$

The Poisson equation is used to find the pressure, at which the velocity at the new time step is divergence free.

## 2.2. Effective heat capacity

Latent heat of fusion, evaporation and latent heat of phase transformations in solid state were considered in capacity model. Effective heat capacity in the mushy zone during solid-liquid phase transformation equals

$$C_{ef}(T) = \begin{cases} \rho_s c_s & \text{for } T < T_S \\ \rho_{sl} c_{sl} - \rho_s H_L \frac{df_s(T)}{dT} & \text{for } T \in [T_S; T_L] \\ \rho_l c_l & \text{for } T > T_L \end{cases} \quad (14)$$

The product of density and specific heat in the mushy zone is calculated with assumption of linear approximation of solid fraction [13, 14]:

$$c_{sl}\rho_{sl} = c_s\rho_s f_s + c_l\rho_l(1 - f_s) \quad (15)$$

Assuming linear approximation of a liquid phase  $f_{l-g} \in [0; 1]$  between boiling point ( $T_b$ ) and maximal temperature appearing in analyzed domain, the volumetric fraction of liquid phase in liquid-gas region is described as follows

$$f_{l-g} = \frac{T_{\max} - T}{T_{\max} - T_b} \quad (16)$$

moreover, the effective heat capacity in temperatures exceeding metal boiling point equals

$$C_{ef} = \rho_l c_l + \frac{\rho_l H_b}{T_{\max} - T_b} \quad \text{for } T \geq T_b \quad (17)$$

Only if full equilibrium of metal vaporisation pressure in the keyhole and pressure of shielding gases is assumed, effective heat capacity model for evaporation is equitable.

Heat capacity of structural constituents of steel and latent heats generated during following phase transformations are determined experimentally [12, 13, 14, 17].

Effective heat capacity after including latent heat of phase transformations equals

$$C_{ef}^{ph} = \begin{cases} \rho_s c_s + \sum_i \rho_s H_i^{\eta_i} \frac{d\eta_i(T)}{dT} & \text{for } T \in [T_s^i; T_f^i] \\ \rho_s c_s & \text{for } T \notin (T_s^i; T_f^i) \end{cases} \quad (18)$$

where  $T_s^i$  and  $T_f^i$  are start and finish temperatures of each phase transformation,  $H_i^{\eta_i}$  is a latent heat of i-th phase transformation,  $\eta_i$  is a volumetric fraction of i-th phase. Latent heats of austenite into ferrite ( $H_{A \rightarrow F}$ ), pearlite ( $H_{A \rightarrow P}$ ), bainite ( $H_{A \rightarrow B}$ ) and martensite ( $H_{A \rightarrow M}$ ) transformation are assumed according to [12, 13].

## 2.3. Electric arc and laser beam heat sources

The heat source produced by the welding torch plays an important role in modelling of arc welding processes. Goldak [18] described ‘double ellipsoidal’ power density distribution of the heat source below the welding arc, which can simulate different types of arc welding and various process parameters. This heat source model has very good features of power density distribution control in the weld and HAZ and is widely accepted by the researchers. Shape of Goldak’s source is a combination of two half-ellipses connected to each other with one semi-axis. Power distribution of this heat source is formulated as follows:

$$Q_1 = \begin{cases} q_1(x, y, z) = \frac{6\sqrt{3}f_1 Q_A}{abc_1 \pi \sqrt{\pi}} \times \exp(-3\frac{x^2}{c_1^2}) \times \exp(-3\frac{y^2}{a^2}) \times \exp(-3\frac{z^2}{b^2}) & \text{for } x < x_o \\ q_2(x, y, z) = \frac{6\sqrt{3}f_2 Q_A}{abc_2 \pi \sqrt{\pi}} \times \exp(-3\frac{x^2}{c_2^2}) \times \exp(-3\frac{y^2}{a^2}) \times \exp(-3\frac{z^2}{b^2}) & \text{for } x \geq x_o \end{cases} \quad (19)$$

where  $a, b, c_1$  and  $c_2$  are set of axes that define front ellipsoid and rear ellipsoid,  $f_1$  and  $f_2$  ( $f_1 + f_2 = 2$ ) represent distribution of the source energy at the front and the rear section of the source, thus resultant distribution of the source energy is total sum described as  $Q_v(x, y, z) = q_1(x, y, z) + q_2(x, y, z)$  and  $Q_A = \eta_1 I U$  is the arc heat source power, where  $I$  is current intensity,  $U$  is voltage and  $\eta_1$  is efficiency of the electric arc.

In the majority of studies concerning laser surface treatment, the laser beam power is considered to be sufficiently low and can be simplified as a surface heating source [6]. In the laser welding process high power laser forms the keyhole and transports the heat below the surface of the workpiece as soon as the beam impinges on the material. According to this specific melting phenomenon accompanying the laser welding process, especially

at a large thickness of welded workpiece, more realistic, cylindrical-involution-normal (CIN) [19] heat source model is proposed.

This heat source distribution allows for modelling of variety concentrated volumetric heat source shapes from parabola to a point taking into account the changes of heat source power density with material penetration depth. The CIN model is represented by the following equation:

$$Q_2(r, z) = \frac{k K_z \eta_2 Q_L}{\pi (1 - e^{(K_z s)})} e^{-(kr^2 + K_z z)} (1 - u(z - s)) \quad (20)$$

where  $Q_L$  is the laser beam power,  $\eta_2$  is the laser efficiency,  $r = \sqrt{x^2 + y^2}$  is the current radius,  $K_z = 3/s$  is the heat source power exponent,  $k = 3/r_0^2$  is the beam focus coefficient,  $r_0$  is a beam radius and  $s$  is heat source beam penetration depth,  $u(z - s)$  is Heaviside function.

In this study hybrid heat source is used in calculations as a product of Goldak's and CIN heat sources. Exemplary hybrid heat source power distribution in geometrical set-up with leading arc is presented in Figure 2 at the top surface of the workpiece and in longitudinal section of the joint in the middle of heat sources activity zone.

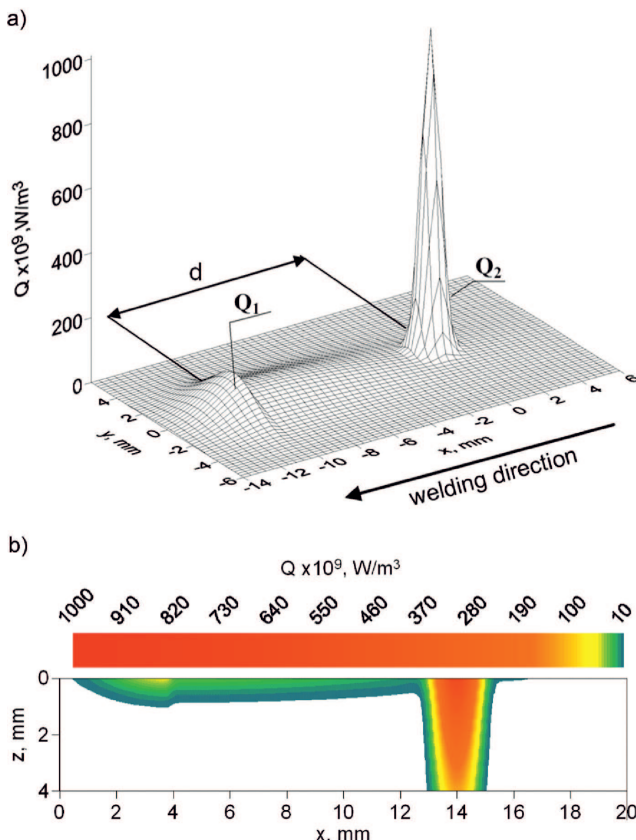


Fig. 2. Exemplary heat source power distribution a) at the top surface of welded joint and b) in longitudinal section, in the middle of heat activity zone

### 3. Phase transformations

The model for prediction of structure composition was defined on the basis of classic mathematical models of kinetics of phase transformation in solid state as well as CHT and CCT diagrams [13, 14, 20, 21] for welded steel. Analysis of phase transformations in welded flat made of S355 steel, with chemical composition: 0.19 C, 1.05 Mn, 0.2 Si, 0.08 Cr, 0.11 Ni, 0.006 Al, 0.028 P, 0.02 S [%] was performed for heating and cooling.

#### 3.1. Heating

Phase transformations during heating are calculated on the basis of JMA formula taking into account the influence of heating rates on austenitization temperatures  $Ac_1(t)$  and  $Ac_3(t)$  (CHT diagram).

$$\tilde{\eta}_A(T, t) = \eta_{(.)}(1 - \exp(-b t^n)) \quad (21)$$

where  $\eta_{(.)}$  is a sum of volumetric fractions of base material structure ( $\eta_{(.)}=1$ ), coefficients  $b = b(T)$  and  $n = n(T)$  are determined by starting ( $\eta_s=0.01$ ) and final ( $\eta_f = 0.99$ ) conditions for phase transformation as follows

$$b(T) = -\frac{\ln(\eta_f)}{(t_s)^{n(T)}}, \quad n(T) = \frac{\ln(\ln(\eta_f)/\ln(\eta_s))}{\ln(t_s/t_f)} \quad (22)$$

where  $t$  is a time,  $t_s = t_s(T_{sA})$  and  $t_f = t_f(T_{fA})$  are phase transformation start and final times,  $T_{sA}$  and  $T_{fA}$  are start and final temperatures.

If maximum temperature of thermal cycle is found between  $[Ac_1 \div Ac_3]$  temperatures, then incomplete austenitization occurs [13, 14]. In this case a fraction of austenite formed during heating equals

$$\eta_A = (T_{\max} - Ac_1(t))/(Ac_3(t) - Ac_1(t)) \quad (23)$$

Base material structure untransformed into the austenite is defined as sum of fractions  $\eta_k = (1 - \eta_A)$ . When incomplete austenitization occurs, aggregated fractions of phases arising during cooling are assumed as a sum of fractions transformed from austenite and reminder untransformed (base material) structure.

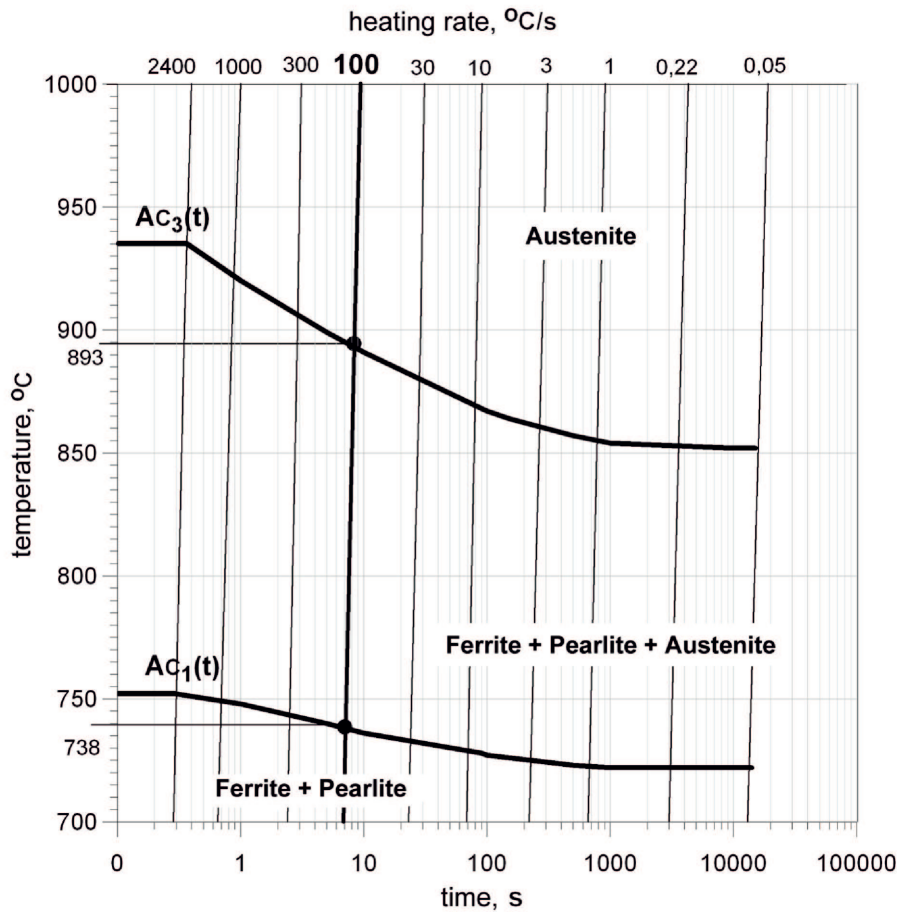


Fig. 3. CHT diagram of S355 steel [21]

### 3.2. Cooling

The volumetric fractions of phases forming from austenite during cooling are determined by temperatures and cooling rates in temperature range [800÷500] °C. A fraction of a new phase growth for diffusive phase transformations such as bainite, pearlite or ferrite, are usually established on the basis of JMA formula taking into account existed phase fractions in equation (21), which leads to the following formula

$$\eta_{(\cdot)}(T, t) = \eta_{(\cdot)}^{\%} \tilde{\eta}_A (1 - \exp(-b(t(T))^n)), \quad (24)$$

$$\underline{\eta}_A - \sum_{k=1}^4 \eta_k \geq 0, \quad \sum_{k=1}^5 \eta_k^{\%} = 1$$

where  $\eta_{(\cdot)}^{\%}$  is the maximal phase fraction for determined cooling rate, estimated on the basis of CCT diagram,  $\tilde{\eta}_A$  is the austenite fraction formed due to heating, while  $\eta_k$  is a phase fraction formed before calculated phase transformation during cooling. Coefficients  $b$  and  $n$  are also calculated from formula (22).

Volumetric fraction of martensite ( $\eta_M$ ) is estimated between start and final temperatures ( $M_s$  and  $M_f$ ), using KM formula

$$\eta_M(T) = \eta_{(\cdot)}^{\%} \tilde{\eta}_A (1 - \exp(-k(M_s - T)^m)) \quad (25)$$

where coefficient  $k$  is expresses as follows

$$k = -\frac{\ln(\eta_s)}{M_s - M_f} = -\frac{\ln(0.01)}{M_s - M_f} \quad (26)$$

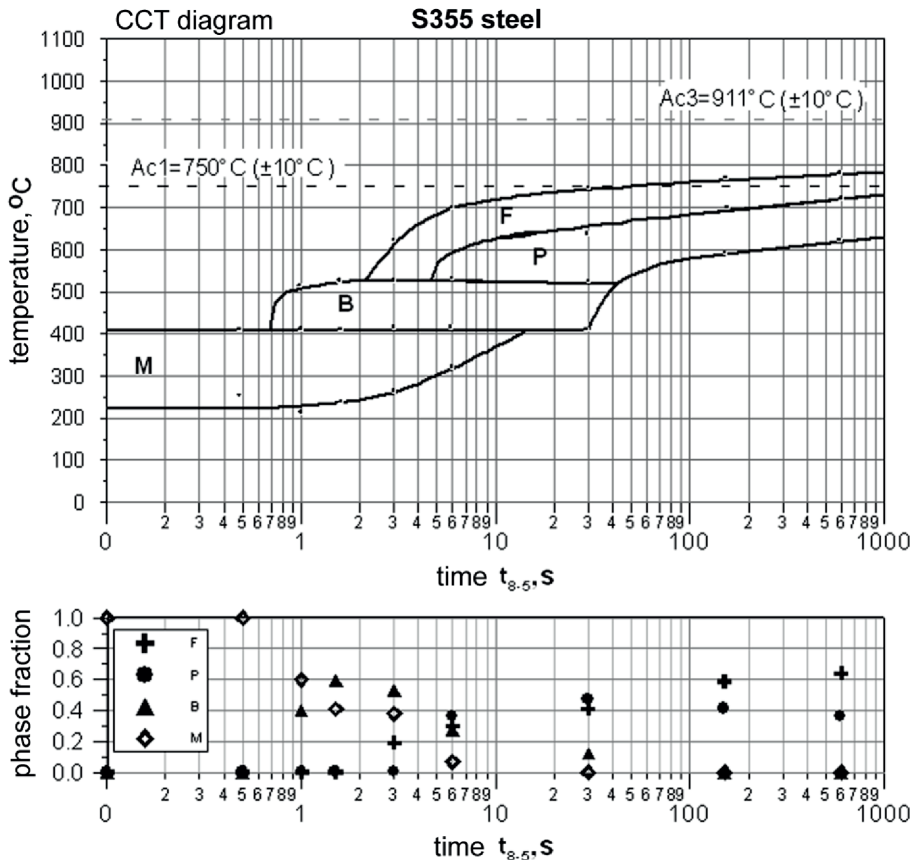


Fig. 4. CCT diagram and phase composition of S355 steel [21]

#### 4. Thermal and structural strain

In analysis of heating and cooling during hybrid welding process, thermal as well as structural strain is calculated [13, 14, 17]. Simulated dilatometric curves are obtained by a solution of the increase of isotropic strain

$$d\epsilon^{Tph} = \sum_{i=1}^{i=5} (\alpha_i \eta_i dT - sgn(dT) \epsilon_i^{ph} d\eta_i) \quad (27)$$

where  $\alpha_A = \alpha_A(T)$  are thermal expansion coefficients of austenite, bainite, ferrite, martensite and pearlite,  $\epsilon_i^{ph} = \epsilon_i^{ph}(T)$  is an isotropic structural strain resulting from the transformation of the base structure into austenite during heating and each phase (ferrite, pearlite, bainite or martensite) arising from austenite during cooling,  $d\eta_i$  is a volumetric fractions of phases,  $sgn(.)$  is a sign function. Thermal expansion coefficients and structural strain were determined on the basis of dilatometric analysis for considered steel [14].

#### 5. Results and discussion

Computer simulation of laser – arc hybrid welding process was performed for  $150 \times 30 \times 4$  mm thin plate made of S355 steel with assumed base material structure consist of ferritic – pearlitic structure (60% ferrite and 40% pearlite), in geometrical set-up with leading electric arc. Shown in table 1 material properties were assumed in numerical calculations. Heat sources parameters were set to: laser beam power  $Q_L = 3800$  W, laser beam radius  $r_0 = 1$  mm, laser efficiency  $\eta_2 = 85\%$ , arc current  $I = 310$  A, welding voltage  $U = 31.8$  V, arc efficiency  $\eta_1 = 75\%$ . Distance between arc torch and laser beam focal point was set to  $d = 5$  mm and welding speed  $v = 2.6$  m/min.

TABLE 1  
Thermo-physical parameters assumed in simulation

Nomenclature	Symbol	Value
Solidus temperature	$T_s$	1750 K
Liquidus temperature	$T_L$	1800 K
Boiling point	$T_b$	3010 K
Ambient temperature	$T_0$	293 K
Specific heat of solid phase	$c_s$	650 J/kgK
Specific heat of liquid phase	$c_L$	840 J/kgK
Density of solid phase	$\rho_s$	7800 kg/m <sup>3</sup>
Density of liquid phase	$\rho_L$	6800 kg/m <sup>3</sup>
Latent heat of fusion	$H_L$	$270 \times 10^3$ J/kg
Latent heat of evaporation	$H_b$	$76 \times 10^5$ J/kg
Latent heat of phase transformations	$H_{A \rightarrow F}$ $H_{A \rightarrow P}$ $H_{A \rightarrow B}$ $H_{A \rightarrow M}$	$8 \times 10^4$ J/kg $9 \times 10^4$ J/kg $11.5 \times 10^4$ J/kg $11.5 \times 10^4$ J/kg
Thermal conductivity of solid phase	$\lambda_s$	45 W/mK
Thermal conductivity of liquid phase	$\lambda_L$	35 W/mK
Convective heat transfer coefficient	$\alpha$	50 W/m <sup>2</sup> K
Boltzmann's constant	$\sigma$	$5.67 \times 10^{-8}$ W/m <sup>2</sup> K <sup>4</sup>
Thermal expansion coefficient	$\beta_T$	$4.95 \times 10^{-5}$ 1/K
Surface radiation emissivity	$\varepsilon$	0.5
Dynamic viscosity	$\mu$	0.006 kg/ms
Solid particle average diameter	$d_0$	0.0001 m

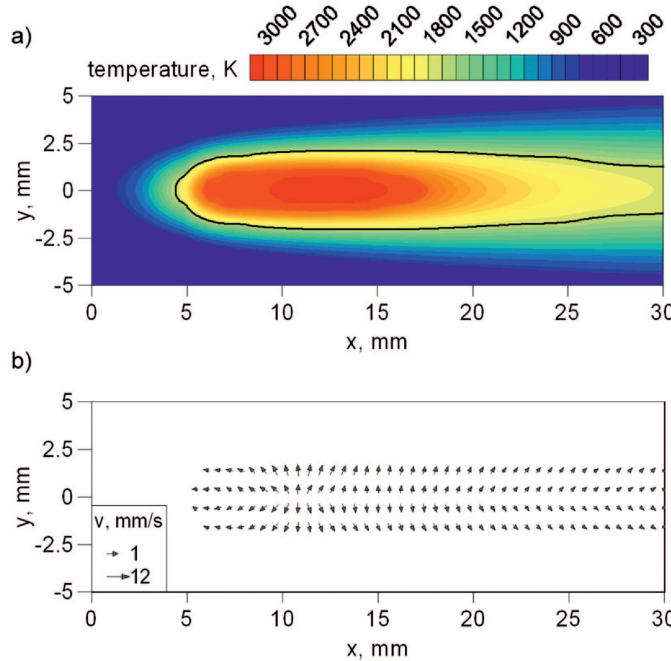


Fig. 5. Calculated a) temperature field and b) velocity field at top surface of welded flat (from the face of the weld)

Figure 5 presents temperature field and melted material velocity field at the top surface of welded flat (from the face of the weld,  $z=0$ ), where solid line (solidus isotherm) determines shape of melted zone. Temperature field and velocity field in the longitudinal section of welded joint are presented in Figure 6.

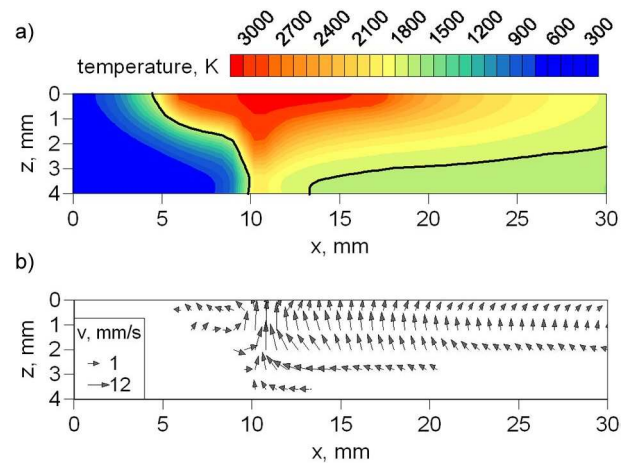


Fig. 6. Calculated a) temperature field and b) velocity field in the longitudinal section of welded flat, in the middle of heat sources activity zone ( $y=0$ )

It can be observed in figure 5 that distance ( $d$ ) between electric arc and laser beam is sufficient for synergy effect due to interaction of both heat sources in the welding pool. As shown in longitudinal section of welded joint (Fig. 6) in this set-up, when electric arc is the leading heat source in tandem, this heat source melts upper parts of the workpiece, which results in better material penetration by the laser beam.

The formation of laser-arc hybrid welded joint is presented in Figure 7. This figure illustrates temperature distribution at different analysis time, where solid line determines melted zone shape and dashed line represents heat affected zone ( $T=Ac_1 \approx 1000$ K). At time  $t=0.1$ s the flat is heated below solidus temperature. When  $t=0.16$ s, electric arc melts upper layers of the workpiece. Maximum size of melted zone and maximum temperatures in the weld are observed at  $t=0.25$ s, where the laser beam fully penetrate welded joint. After this time, the joint is cooled to the ambient temperature reaching maximum size of heat affected zone at  $t=0.47$ s.

Numerically calculated velocity field of melted steel in the welding pool is illustrated in Figure 8. It is observed that motion of melted material in the welding pool has a significant influence on the weld shape and maximum velocity is reached in the middle of heat sources activity zone.

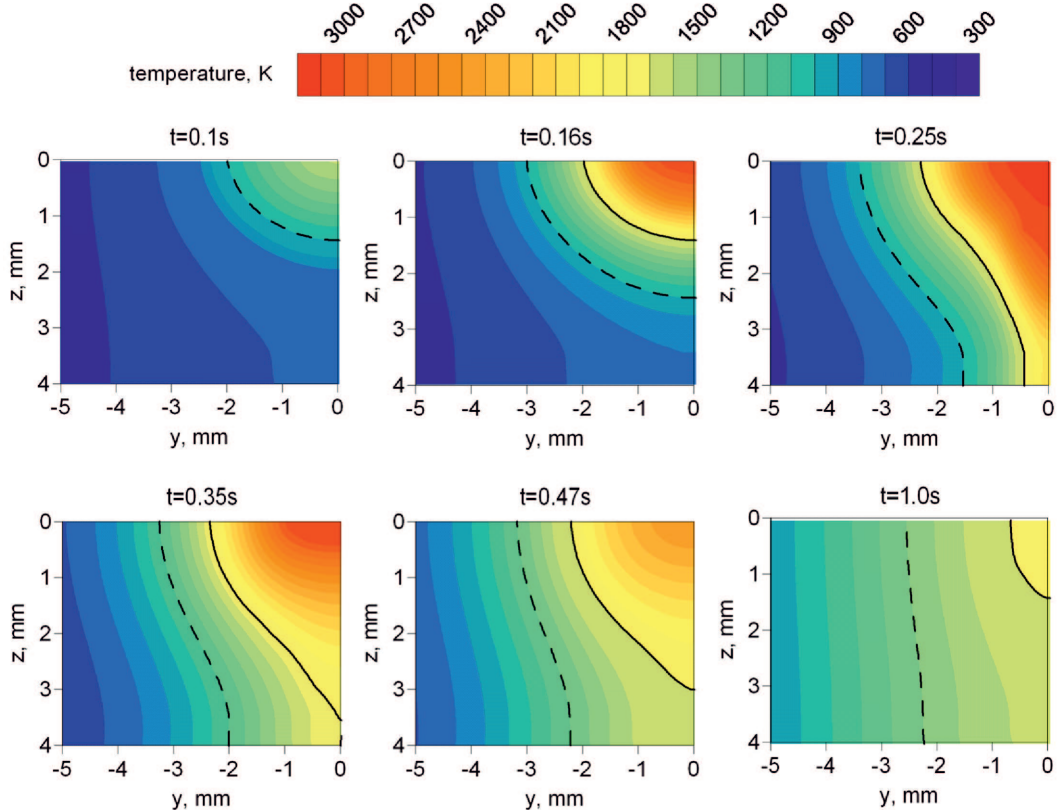


Fig. 7. Temperature distribution in the cross section of welded joint at different time

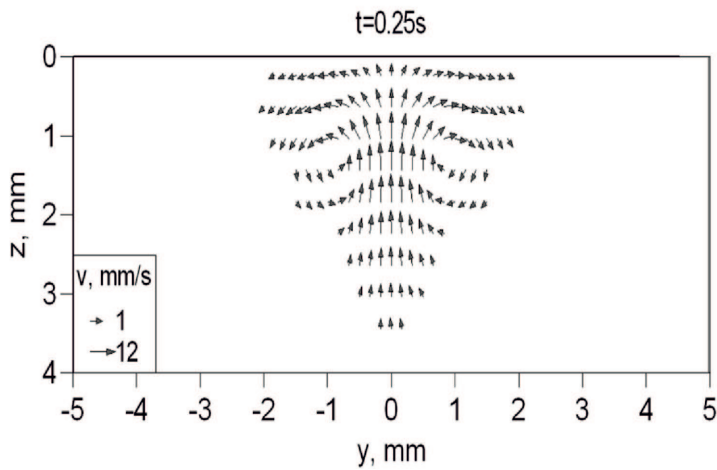


Fig. 8. Velocity field in the cross section of welded joint at the time  $t=0.25s$

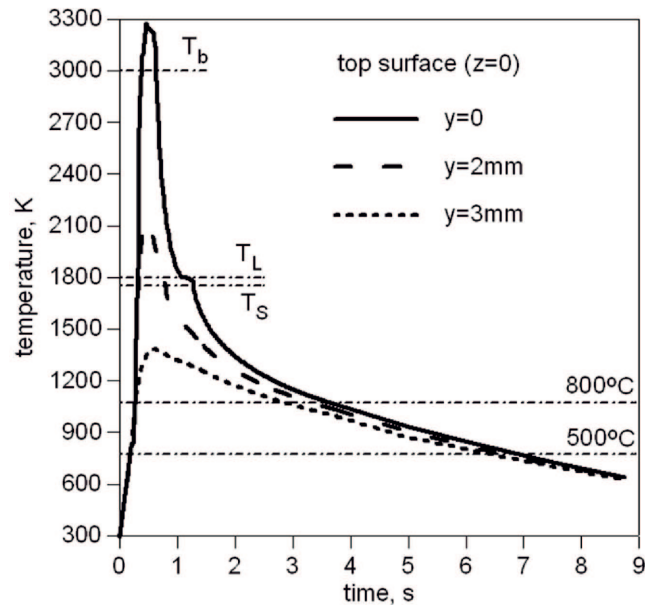


Fig. 9. Thermal cycles at the top surface of the flat (from the face of the weld)

Figure 9 presents thermal cycles for chosen points at the top surface of the flat ( $z=0$ ), with marked solidus, liquidus and boiling temperatures as well as the temperatures range [800÷500] °C where cooling rate ( $v_{8/5}$ ) for each thermal cycle is determined. The noticeable changes in temperature distribution are observed between  $T_S$  and  $T_L$  resulting from solidification of steel.

On the basis of obtained thermal cycles, the kinetics of phase transformation is analyzed during simulation of laser-arc hybrid welding. Figure 10 shows kinetic of phase transformations at the top surface of

the weld for a chosen thermal cycle where cooling rate equals  $v_{8/5}=68 \text{ K/s}$ . Figure 11 presents calculated isotropic strain corresponding to this kinetic of phase transformations.

Numerically predicted volumetric fractions of pearlite, ferrite, bainite and martensite in cross section of the weld are illustrated in Figure 12. As shown in this figure, predicted martensite structure is up to 20%, because of the lower cooling rates occurring in laser-arc hybrid welding process.

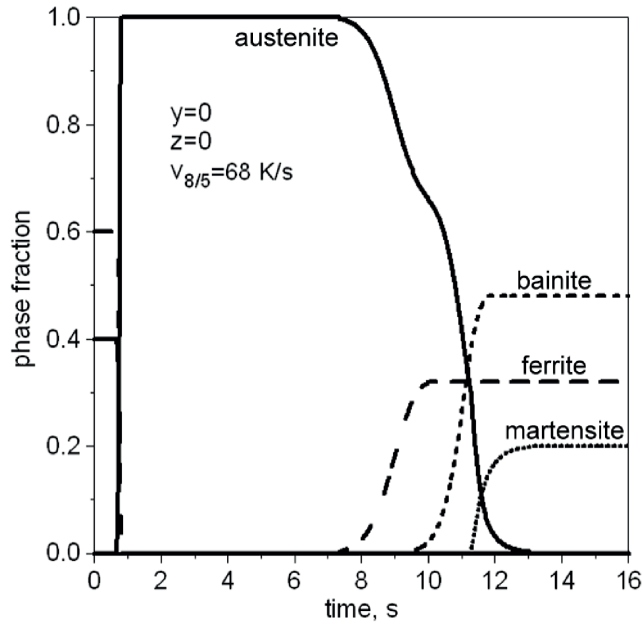


Fig. 10. Kinetics of phase transformations for thermal cycle at a point  $y=0, z=0$

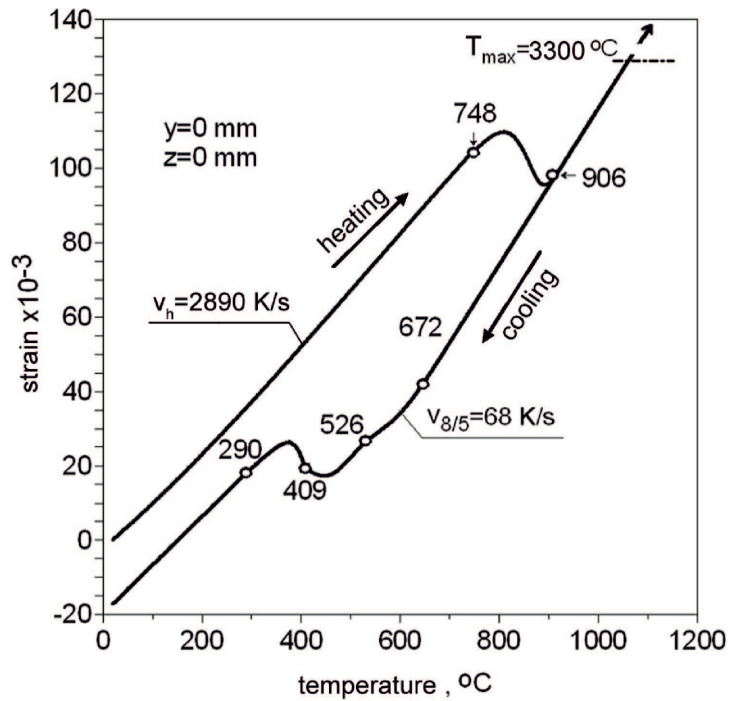


Fig. 11. Simulated thermal and structural strain for thermal cycle at a point  $y=0, z=0$

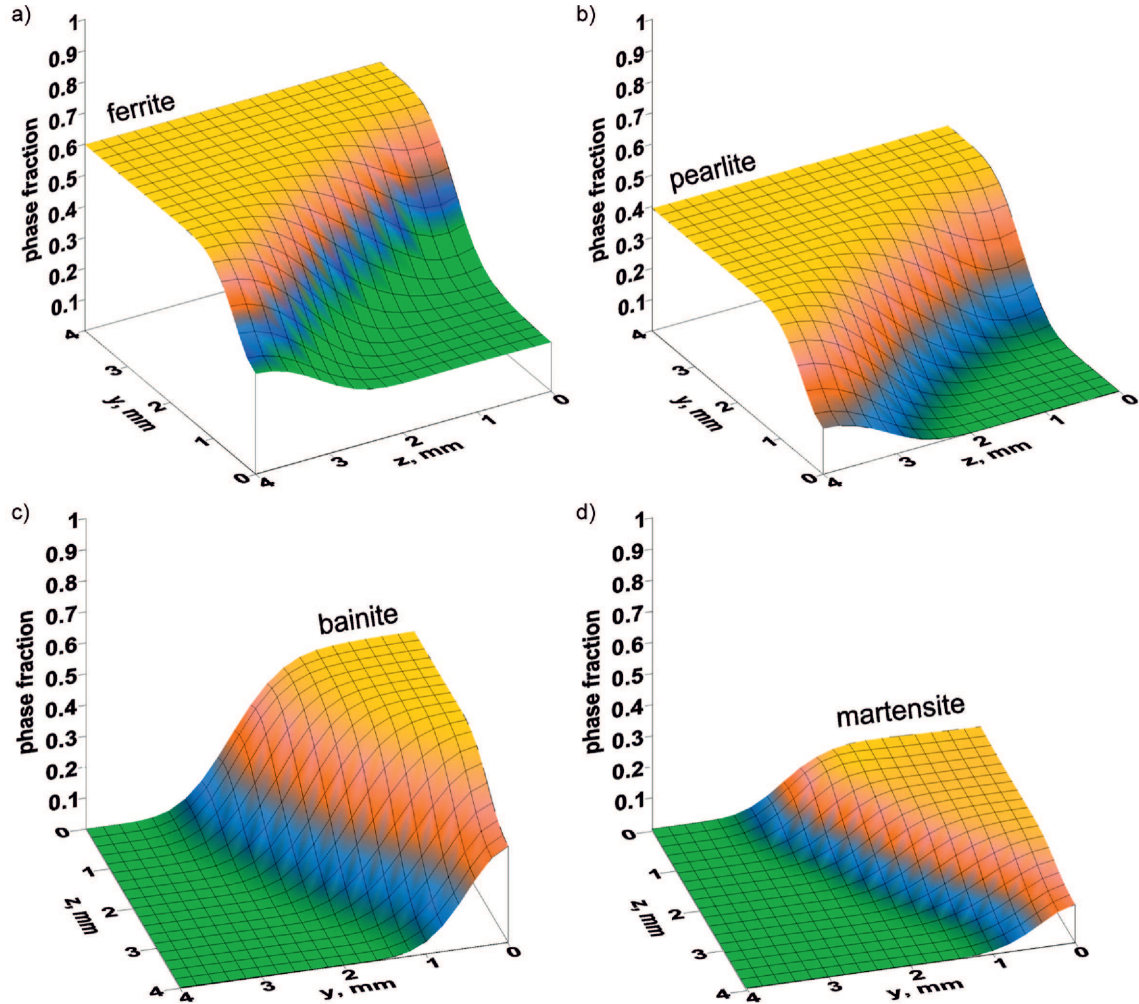


Fig. 12. Numerically estimated structure composition in hybrid welded joint, a) ferrite, b) pearlite, c) bainite and d) martensite

Process parameters used in experiment

TABLE 2

Welding speed	Laser-to-arc distance	MIG/MAG	Laser
$v = 2.6 \text{ m/min}$	$d \approx 5\text{mm}$	$I=310\text{A}, U=31.8 \text{ V}$ shielding gas: argon/helium (50% / 50%) 12 l/min, feed rate: 10 m/min	$Q_L = 3800\text{W}$ shielding gas: helium 8 l/min

The results of numerical analysis were compared to Laser-MIG welding, performed in Welding Institute in Gliwice for a flat made of S355 steel with the same dimensions used in computer simulations. In the experiment CO<sub>2</sub> laser was used and semi-automatic welder with MIG/MAG welding torch. The laser and semi-automatic welder were precisely set together with the use of cruciform table made of linear slides with 1mm accuracy. Welding torch angle was set up by rota-

tional module with 1deg. accuracy. Process parameters used in experiment are described in Table 2.

Numerically predicted martesite constituent in the cross section of welded joint compared to macroscopic picture of the weld is illustrated in Figure 13.

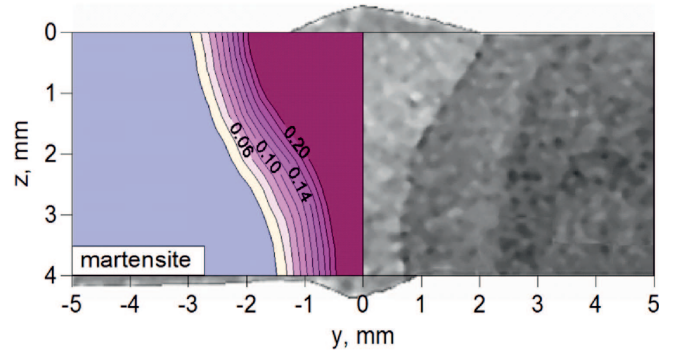


Fig. 13. Martensite distribution in the cross-sectional area of hybrid welded joint

## 6. Conclusions

Described three-dimensional model takes into account the thermal phenomena including coupled heat transfer with convective motion of liquid material in the welding pool, latent heat associated with material's state changes and latent heat of phase transformations in solid state. On the basis of numerical solutions of described mathematical models, computer simulation of hybrid welding process was performed.

The results of numerical analysis were presented in this paper including temperature field, velocity field of melted steel in the welding pool and numerical predicted structural composition of butt-welded flat made of higher-strength S355 steel. Transient heat transfer equation was solved numerically by finite element method in Petrov – Galerkin formulation and Navier – Stokes equation was solved using Chorin's projection method. The solution algorithms were implemented in ObjectPascal programming language.

On the basis of presented results of numerically calculated temperature field it can be stated that the technological parameters of laser-arc hybrid welding used in calculations contribute to considerable melting of the material by an electric arc. Laser beam was used mainly to increase material penetration depth, formed previously by the electric arc, which is confirmed by velocity field of liquid metal in the welding pool (Fig. 5, 6, and 8). It can be noticed that liquid metal motion is intense, not only at the top, but also at the bottom layers of welded joint and the circulation of liquid metal in the melted zone produced by the electric arc has a great influence on the width of welding pool at the top surface of the joint (from the face of the weld). Near the heat source activity zone slight evaporation of steel occurs (Fig. 10). Comparison of the results of calculations (Fig. 7) with the experiment (Fig. 13) shows the correctness of assumed solution method and satisfactory accuracy of obtained results of temperature field and characteristic zones of the weld. The various temperatures result in miscellaneous structure composition of the joint (Fig. 12). It is noted that after laser-arc hybrid welding the material in weld and heat affected zone is partially hardened.

Presented mathematical and numerical models of thermal phenomena and phase transformations in solid state allow for the analysis of important process parameters, such as relative arrangement of heat sources and the selection of heat sources power. It should be noticed that it is possible to select optimal technological parameters and determine their influence on the quality and durability of welded joint for specified steel.

## REFERENCES

- [1] C. Bagger, F.O. Olsen, Review of laser hybrid welding, *Journal of Laser Applications* **17** (2005).
- [2] U. Dilthey, A. Wieschemann, Prospects by combining and coupling laser beam and arc welding processes, *Welding in the World* **44**, 37-46 (2000).
- [3] J. Pilarczyk, M. Banasik, J. Dworak, S. Stano, Hybrid welding using laser beam and electric arc, *Przeglad Spawalnicza* **10**, 44-48 (2007) (in polish).
- [4] M. Wouters, Hybrid laser-MIG welding: An investigation of geometrical considerations, Lulea, Sweden (2005).
- [5] P. Seyffarth, I.V. Kriwtsun, *Laser-Arc Processes and their Applications in Welding and Material Treatment*, Taylor & Francis, USA (2002).
- [6] J.M. Dowden, *The mathematics of thermal modeling*, Taylor & Francis Group, USA (2001).
- [7] J.H. Cho, S.J. Na, Three-Dimensional analysis of molten pool in GMA-Laser hybrid welding, *Welding Journal* **88**, 35-43 (2009).
- [8] J. Zhou, H.L. Tsai, Modeling of transport phenomena In hybrid laser – MIG keyhole welding, *International Journal of Heat and Mass Transfer* **51**, 4353-4366 (2008).
- [9] W.S. Chang, S.J. Na, A study on the prediction of the laser weld shape with varying heat source equations and the thermal distortion of a small structure in micro-joining, *Journal of Materials Processing Technology* **120**, 208-214 (2002).
- [10] X. Jin, L. Li, Y. Zhang, A study of fresnel absorption and reflections in the keyhole in deep penetration laser welding, *Journal of Physics D: Applied Physics* **35**, 2304-2310 (2002).
- [11] B. Nedjdar, An enthalpy-based finite element method for nonlinear heat problems involving phase change, *Computers & Structures* **80**, 9-21 (2002).
- [12] K.J. Lee, Characteristics of heat generation during transformation in carbon steels, *Scripta Materialia* **40**, 735-742 (1999).
- [13] W. Piekarzka, Numerical analysis of thermomechanical phenomena during laser welding process. The temperature fields, phase transformation and stresses, Wydawnictwo Politechniki Częstochowskiej, Częstochowa (2007) (in polish).
- [14] M. Kubiać, Numerical modeling of thermal phenomena in hybrid welding process, PhD thesis, Częstochowa University of Technology, Częstochowa (2010) (in polish).
- [15] O.C. Zienkiewicz, R.L. Taylor, *The finite element method*, Butterworth-Heinemann, Fifth edition **1,2,3**, USA (2000).
- [16] S.V. Patankar, *Numerical heat transfer and fluid flow*, Taylor & Francis, USA (1990).
- [17] A. Bokota, T. Domanski, Numerical analysis of thermo-mechanical phenomena of hardening process of elements made of carbon steel C80U, *Archives of Metallurgy and Materials* **52**, 2, 277-288 (2007).

- [18] J.A. Goldak, Computational Welding Mechanics, Springer USA (2005).
- [19] E. Ranatowski, Thermal modelling of laser welding. Part I: The physical basis of laser welding, *Advances in Materials Science* **1**, 34-40 (2003).
- [20] W. Zhang, B. Wood, T. DebRoy, J.W. Eimer, T.A. Palmer, Kinetic modeling of phase transformations occurring in the HAZ of C-Mn steel welds based on direct observations, *Acta Materialia* **51**, 3333-3349 (2003).
- [21] J. Orlich, H. J. Pietzenik, *Atlas zur Wärmebehandlung der Stähle*: **3**, Dusseldorf (1973).

Received: 10 January 2011.